RESEARCH ARTICLE

ADVANCED MATERIALS INTERFACES Open Access

www.advmatinterfaces.de

Strain Relief and Domain Architecture in Epitaxial NiO Films on $La_{2/3}Sr_{1/3}MnO_3/SrTiO_3$ for Spin-Transport Engineering

*Shoulong Chen, Carlos Frontera, Meritxell Toda-Casaban, Alberto Pomar, Lluis Balcells, Zorica Konstantinovic, Cesar Magén, Benjamin Martinez, and Narcis Mestres**

This study reports on the epitaxial growth and structural characterization of ultrathin NiO-films deposited by magnetron sputtering on $La_{2/3}Sr_{1/3}MnO_3$ (LSMO) films grown on $SrTiO_3$ (STO) substrates with (001)- and (111)-orientations. X-ray diffraction and atomic-force microscopy show that all NiO layers are single-phase, face-centered pseudo-cubic, atomically smooth, root-main-square (RMS) surface roughness <0.15 nm, and form abrupt interfaces with LSMO. High-resolution reciprocal-space maps reveal that the films are largely relaxed, but exhibit a slight compressive distortion, yielding unit-cell volumes larger than bulk NiO. Despite a nominal ≈7% lattice mismatch, aberration-corrected scanning transmission electron microscopy uncovers an array of misfit dislocations at the NiO/LSMO interface that help to accommodate strain allowing epitaxial growth of NiO layers. On (001)-oriented samples, the four antiferromagnetic T-domains are oblique to the sample plane, while on the (111) case, one lies in-plane. This in-plane domain shows greater spacing between ferromagnetic (111) planes due to unit cell distortion. This structural domain splitting can influence magnetic order and spin transmission efficiency, highlighting crystallographic orientation as a key factor in designing high-performance spintronic devices.

1. Introduction

The emerging field of antiferromagnetic (AF) spintronics is regarded as one of the most promising avenues for next-generation energy-efficient, high-speed, and robust information storage and processing technologies. Antiferromagnets offer several key advantages over ferromagnets (FM): they support faster dynamics due to terahertz-range resonance frequencies, feature antiparallel spin sublattices that produce no net dipolar fields thus, rendering them immune to external magnetic field disturbances, and allow for higher data density due to the absence of stray magnetic fields.[1,2] Recent studies have focused on the ability to generate, transport, and detect spin currents in AF insulators.[3–5] In these materials, spin transport occurs via magnon currents, therefore avoiding Joule heating. This makes magnon-based devices attractive for low-power information transmission. AF insulators have proven especially suitable for exciting and guiding magnons. These AF magnons can be excited both thermally and through resonant techniques. They are capable of transmitting spin information across distances of several tens of microns and can be switched on or off by altering the magnetic states of the AF material.[6,7]

Among insulating AF materials, NiO, with a bulk Néel temperature of $T_N = 523$ K, has been extensively studied due to its simple crystal structure and, in principle, relatively straightforward AF ordering. Being electrically insulating, NiO provides a path for spin transport that does not rely on itinerant electrons. However, the precise mechanisms and efficiency of spin conduction in NiO remain under debate.[8] In this context, the role of AF as insertion barriers in FM/normal metal (NM) bilayers, such as in $Y_3Fe_5O_{12}$/NiO/Pt heterostructures, has been intensively studied. The question of whether the inclusion of a NiO layer enhances or hinders spin current transmission under certain circumstances remains highly controversial and needs to be clarified.[9–11] In particular, key aspects of the microstructure of AF layers, such as whether they are polycrystalline or epitaxial, along with their crystallographic orientation, remain poorly understood. Closely related to this is the issue of the orientation of the Néel vector that can facilitate or hinder the transmission of spin currents.[12]

S. Chen, C. Frontera, M. Toda-Casaban, A. Pomar, L. Balcells, B. Martinez, N. Mestres
Institut de Ciència de Materials de Barcelona
ICMAB-CSIC
Campus Universitari UAB
Bellaterra, Cerdanyola 08193, Spain
E-mail: narcis.mestres@icmab.es

Z. Konstantinovic
Center for Solid State Physics and New Materials
Institute of Physics Belgrade
University of Belgrade
Belgrade 11000, Serbia

C. Magén
Instituto de Nanociencia y Materiales de Aragón (INMA)
CSIC-Universidad de Zaragoza
Zaragoza 50009, Spain

The ORCID identification number(s) for the author(s) of this article can be found under https://doi.org/10.1002/admi.202500452

DOI: 10.1002/admi.202500452

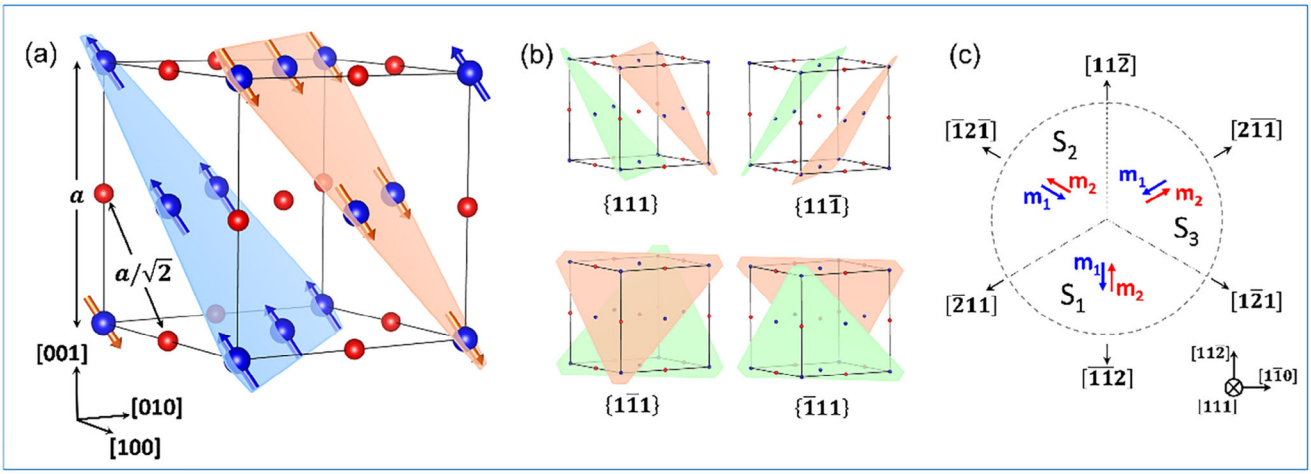

Figure 1. a) NiO crystal structure. The red oxygen ions are centered on the edges and in the cube, and the nickel ions (in blue) are in the corners and the center of each face. The red and blue shadows show the {111} planes with parallel-oriented Ni spins. In b) the four different twin domains T1, T_3 and T_2, T_4 are shown which corresponds to the {111}, {1-11} and {-111}, {11-1} planes respectively. c) NiO domain structure with three domains S_1 – S_2 – S_3 in the {111} planes. Each domain consists of two magnetic sublattices $\mathbf{m_1}$ (blue) and $\mathbf{m_2}$ (red), pointing in the indicated easy directions.

All these aspects are expected to significantly influence long-range AF ordering, interfacial coupling, and spin current enhancement. However, their precise effects on spin transport and interfacial dynamics remain largely unexplored and warrant further investigation. In this sense, it is of great interest to study heterostructures other than $Y_3Fe_5O_{12}$/NiO/Pt that allow epitaxial growth of NiO thin films. For this purpose, we have chosen the system $La_{2/3}Sr_{1/3}MnO_3$ (LSMO)/Pt. LSMO is the archetypal FM manganite with the highest Curie temperature (T_C ≈360 K in thin films), low intrinsic magnetic damping, and high carrier spin polarization.[13–16] It also provides a good lattice match with the common STO substrates for functional oxides growth. To investigate the influence of NiO's crystallographic growth direction, we employed (001)- and (111)-oriented STO substrates. These orientations were chosen because growth along the (111) plane may favour an in-plane alignment of the Néel vector in contrast to (001)-oriented NiO films, which typically exhibit a multidomain magnetic structure with Néel vectors from different T-domains oriented obliquely to the film surface. Achieving a well-defined Néel vector orientation is crucial for probing the coupling between FM and AF layers, which underlies the effective transmission of spin angular momentum.[17] This work presents a detailed investigation of the AF/FM interface in oxide heterostructures, motivated by their potential in spintronic applications. We have investigated in deep how local microstructure and symmetry influence interfacial properties by growing epitaxial LSMO/NiO/Pt trilayers on both (001)- and (111)-oriented STO substrates. To characterize their microstructure, we used X-ray diffraction (XRD) and synchrotron-based measurements to quantify symmetry and epitaxial strain, and high-resolution scanning transmission electron microscopy (STEM) to assess interface sharpness, defect populations, and local chemistry. The results reveal that crystallographic orientation significantly influences the symmetry and atomic stacking at the interface, which in turn governs the orientation of the T domains relevant to spin transport. In (001)-oriented samples, the T domains are oriented obliquely to the film surface, whereas in (111)-oriented samples, in principle, a part of the T domains align in-plane, an arrangement that can boost spin transmission perpendicular to the film plane (See Figure S1, Supporting Information).[18]

1.1. NiO Material Properties

NiO is a well-known collinear AF insulator with a bulk Néel temperature (T_N) of 523 K.[19] It adopts a face-centered cubic (FCC) crystal structure, similar to that of sodium chloride. In this structure, AF superexchange interactions occur between Ni^{2+} ions (depicted blue in **Figure 1a**) via oxygen atoms, forming Ni–O–Ni bonds along the <100> directions.[20] These interactions lead to an FM spin alignment within the {111} planes. Below T_N, Ni^{2+} magnetic moments adopt an AF arrangement, aligning in an alternating up–down sequence along any ⟨111⟩ crystallographic direction.

As a result, the Ni^{2+} ions form two interpenetrating magnetic sublattices with oppositely oriented spins, each lying perpendicular to the propagation vector of the antiferromagnetic ordering. This AF arrangement is accompanied by a subtle structural distortion along the ⟨111⟩ directions due to exchange striction, which causes a symmetry reduction from cubic to rhombohedral.[21] Consequently, twinned crystal domains form within the NiO crystal. This twinning gives rise to four distinct magnetic twin domains—T1, T2, T3, and T4—as illustrated in Figure 1b.[22,23] Although this distortion breaks the ideal cubic symmetry, the in-plane lattice spacing variation remains minimal, ≈0.1% at 300 K. Within each T domain, three magnetically easy axes exist along the <112> directions, giving rise to three possible spin domains (S domains), and leading to a total of 12 different spin configurations.[24] For instance, in the (111) T1 domain, the ⟨1$\bar{1}$2⟩ directions correspond to the magnetic easy axes. Accordingly, in the absence of an external magnetic field (H) and at temperatures below T_N, NiO hosts three AF spin domains (S1, S2, and S3). In each of these domains, spins alternate in direction between neighboring {111} Ni planes (see Figure 1c). Each

domain comprises two magnetic sublattices with opposing magnetizations, $\mathbf{m}_1$ and $\mathbf{m}_2$. The Néel vector, $\mathbf{n}$, that characterizes the AF ordering is defined by $\mathbf{n} = \mathbf{m}_1 - \mathbf{m}_2$.

The bulk lattice constant of NiO is measured at $a = 4.177$ Å (from JCPDS NO. 47–1049 card), while the distance between two oxygen ions (shown in red in Figure 1a) within the {111} planes is $a/\sqrt{2} = 2.954$ Å. The exchange field $\mu_0 H_{ex}$ and the anisotropy field $\mu_0 H_a$ for NiO are reported to be 968.4 T and 11 mT, respectively.[25]

2. Results and Discussion

2.1. Epitaxial NiO on LSMO

One of the most promising and immediate applications of AFs is their function as insertion barriers in FM/NM bilayer systems. In this configuration, AFs play a key role in tuning the interfacial spin transparency (T_{int}), thereby improving spin transfer efficiency between layers. The FM/NiO/NM trilayer structure—commonly using platinum as the NM layer—offers a particularly accessible platform for investigating spin transport through NiO. In such setups, a pure spin current is generated in the FM layer via ferromagnetic resonance (FMR) and injected into the NiO layer (See Figure S1, the Supporting Information). The resulting transverse voltage signal, arising from the inverse spin Hall effect (ISHE), is then detected across the platinum film.[26] As bulk material, LSMO is rhombohedral (space group R-3c) with hexagonal lattice parameters $a = 5.4957$ Å and $c = 13.3713$Å (ICSD, Collection Code 156020); equivalent to $\alpha = \beta = \gamma = 90.26°$, and $a_{bulk} = 3.873$ Å in the trigonal (pseudocubic) cell. To achieve oriented growth of NiO thin films on top of ferromagnetic LSMO, we utilized (001)- and (111)-oriented STO substrates to compare their structural similarities and differences.

On TiO_2-terminated (001)-oriented STO surfaces, the atomic planes parallel to the surface contain both Ti and O atoms. When LSMO thin films are coherently grown on these (001)-oriented cubic STO substrates, the formation of structural domains, or twinning, is commonly observed. This behavior arises from the relaxation of shear strain within the distorted rhombohedral lattice of LSMO as it conforms to the underlying cubic symmetry of STO.[27,28] Nevertheless, for the purposes of our initial analysis, LSMO can be approximated as having a cubic structure, adopting a pseudo-cubic lattice constant of 3.873 Å. The nominal lattice mismatch between LSMO and the cubic STO (001) substrate is ≈0.85%. Given this relatively small mismatch, we expect that the 15 nm thick LSMO films will grow fully strained on the (001)-oriented STO substrate,[29] as will be further discussed. When NiO ($a^{NiO} = 4.177$Å) is grown in a cube-on-cube fashion on fully strained (001)-oriented LSMO/STO ($a_{ip}{}^{LSMO} = a^{STO} = 3.905$Å), it faces a large nominal lattice mismatch of ≈7% with the underlying LSMO.

In contrast, the (111) plane of STO presents a hexagonal symmetry, with its low-index directions lying along [1-10] and [01-1]. It happens that the rhombohedral distortion of bulk LSMO results from a compression along the (111) pseudocubic direction. This means that the parameters in the plane perpendicular to this compression are comparatively "larger" than those in the compression direction. The consequence of this, in combination with the tensile strain introduced by STO is twofold. First, lattice mismatch reduces if the "larger" parameters of LSMO accommodate in-plane. This means that (111) planes of LSMO ((001) planes in the hexagonal cell) are expected to be parallel to (111) STO planes (substrate surface). Second, when LSMO is deposited on (111)-oriented STO, the mismatch reduces to $\epsilon \simeq 0.5\%$ and the biaxial Young's modulus remains isotropic. Moreover, because the (111) substrate plane has three-fold rotational symmetry, any in-plane shear or stretch variants of that distortion are equivalent under 120° rotations. As a result, there is only one symmetry-distinct way for the lattice to accommodate the ≃0.5% tensile strain, eliminating the multiple, inequivalent distortion choices (and thus twin domain formation) that occur on (001)-oriented substrates.[30] Consequently, (111)-oriented LSMO films on STO are expected to grow fully tensile-strained with in-plane magnetization and, unlike their (001)-oriented counterparts, to form without twinned domains.[31] Moreover, we must consider that in (111)-NiO, the lattice planes parallel to the substrate surface consist of Ni or O atoms. However, in (001)-NiO, the lattice planes parallel to the substrate surface have a mixture of Ni and O atoms (see Figure 1a).

Aberration-corrected STEM was employed to analyze the structural properties of the heterostructures, with a particular focus on the NiO layers. **Figure 2**a,b show high-angle annular dark-field (HAADF) images of samples featuring a 1-nm-thick NiO layer on top of epitaxial LSMO(15 nm)/STO for both substrate orientations. Due to the significant difference in the average atomic numbers of the three layers, the contrast has been artificially adjusted to allow simultaneous visualization of the NiO, Pt, and LSMO layers. The images clearly demonstrate the single-crystalline quality of the LSMO underlayer, as well as that of the NiO and Pt layers. In addition, pictures also make evident the atomic sharp interfaces between LSMO and NiO.

Notably, the crystalline and interfacial quality of the LSMO/NiO/Pt heterostructures seems to be very much alike for both crystallographic orientations. The images also clearly show that the NiO layers are continuous, forming a conformal coating over the LSMO layer despite some surface roughness. Pictures make evident that, regardless of a nominal lattice mismatch of ≈7%, the NiO films grow epitaxially on both substrate orientations. This may be explained by the formation of misfit dislocations that appear directly at the interface, which serve to relieve the epitaxial strain.[32] This behavior is evidenced by the high-resolution TEM images depicted in Figure 2c,d. These images reveal a coherent cationic interface between NiO and LSMO along both the (001) and (111) crystallographic planes (Figure 2c,d, respectively). Notably, no transition layers or amorphous regions are observed at the interface. A high density of misfit dislocations is present in both configurations, with average dislocation spacing of 5.1 ± 1.2 Å for the (001)-oriented films and 3.8 ± 0.8 Å for the (111)-oriented ones. The experimental results show that the significant lattice mismatch is addressed by interfacial dislocations.

The DC magnetic properties of the heterostructures were studied by using SQUID magnetometry. In agreement with the very high crystalline quality of LSMO films, a saturation magnetization of $M_S \approx 3.5\ \mu_B\ Mn^{-1}$, close to the theoretical value, and T_C slightly above 350 K were observed in all the samples,

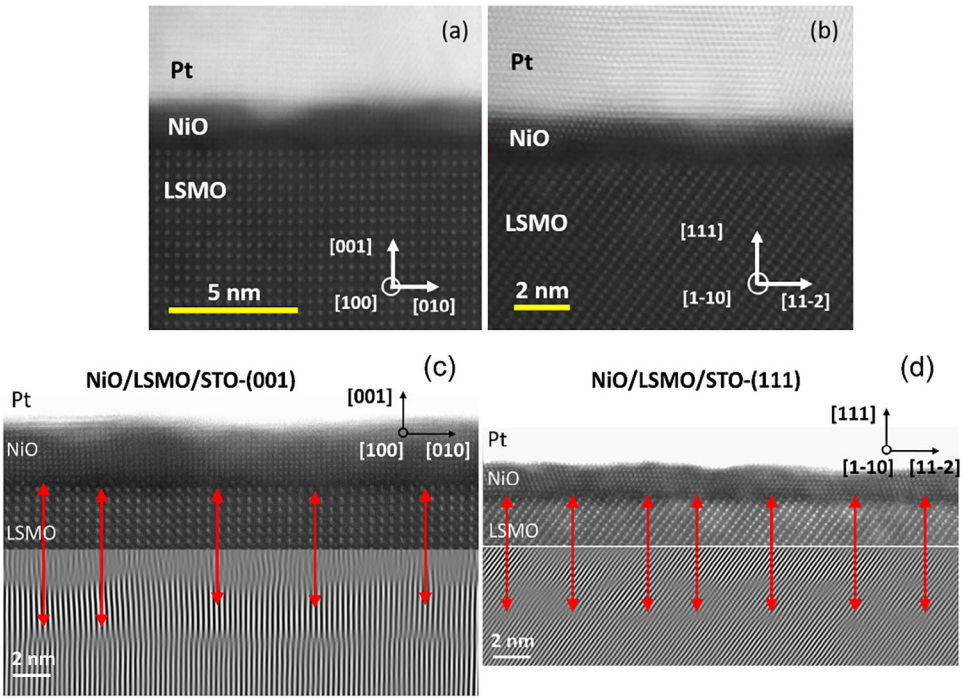

Figure 2. Cross-sectional HAADF-STEM images of a) Pt/NiO/LSMO(15 nm)/STO(100) with a 1 nm-thick NiO layer and b) Pt/NiO/LSMO(15 nm)/STO(111) with a 1 nm-thick NiO layer. The corresponding scale bars and zone axes are also indicated. c)Top: atomic-resolution STEM-HAADF image of the interface LSMO(15 nm)/NiO (2 nm) region, films grown on (001)-STO. Bottom: Fourier filtered image, obtained by [100] diffraction reflection from the STO substrate and NiO epilayer, outlining the common (020) planes between the film and the substrate. d) Top: atomic-resolution STEM-HAADF image of the interface LSMO(15 nm)/NiO (2 nm) region, films grown on (111)-STO. Bottom: Fourier filtered image, obtained by [001] diffraction reflection from the STO substrate and NiO epilayer, outlining the common (002) planes between the film and the substrate. Misfit dislocations localized at the interface are highlighted, the average distance between dislocations is 5.1 Å in (c) and 3.8 Å in (d).

irrespective of the growth crystallographic direction and the NiO layer thickness. The AF ordering of NiO was examined through exchange bias field measurements (see Figure S2, Supporting Information).

2.2. XRD Characterization

2.2.1. Theta-2theta Scans

To verify the epitaxial growth of NiO on LSMO/STO, the XRD technique was used. **Figure 3a** shows θ-2θ out-of-plane scans corresponding to NiO(25 nm)/LSMO(15 nm)/ STO heterostructures, showing only the Bragg peaks corresponding to the STO substrate, LSMO layer, and NiO overlayer. The total absence of unwanted secondary phases is evident. In the top spectrum plotted in red, the (002) reflections of the (001)-STO substrate and LSMO film appear next to the (002) NiO peak, confirming that the [001] crystallographic axis of NiO is locked parallel to the [001] direction of both LSMO and STO. Using the (002) peak position of NiO and applying Bragg's law gives an out-of-plane lattice parameter of $a_{\perp}^{NiO} = 4.249$ Å, which is larger than the lattice constant of bulk NiO of $a_{\perp}^{NiO} = 4.177$ Å, indicating that the NiO film may be under compressive strain.

In the lower (green-traced) θ–2θ scan of Figure 3a, the (111) reflections of the STO substrate, the LSMO layer, and the NiO overlayer all appear, confirming that NiO [111] grows parallel to the [111] directions of both LSMO and STO. To further assess film crystallinity, we performed reciprocal-space mapping with a 2D general area detector diffraction system (GADDS). The absence of Debye–Scherrer arcs in Figure 3b,c demonstrates a single-crystal like texture, and only the NiO (200) peak for films on (001)-STO and the NiO (111) peak for films on (111)-STO are detected. 1D θ–2θ profiles extracted from GADDS (Figure 3d) closely match the high-resolution scans of Figure 3a, though substrate and LSMO peaks appear slightly broadened due to GADDS's lower angular resolution. Using Bragg's law on the NiO (111) reflection at $2\theta = 36.67°$ yields an interplanar spacing $d_{(111)} = 2.449$ Å. For bulk NiO ($a = 4.177$ Å), $d_{(111)} = a_{\mathrm{NiO}}/\sqrt{3} \simeq 2.417$ Å, so the expanded spacing in our 25 nm NiO films indicates compressive strain when grown on LSMO/(111)-STO. Atomic-force microscopy (AFM) topographs of Pt/NiO(1 nm)/LSMO(15 nm)/(001)-STO and Pt/NiO(1 nm)/LSMO/(111)-STO (Figure 3e,f) reveal RMS surface roughnesses of 0.15 and 0.14 nm, respectively, confirming atomically flat surfaces in both orientations.

2.2.2. Pole Figures

To probe the films' symmetry and epitaxial alignment, we conducted off-axis φ-scans on both NiO and STO reflections. For NiO films deposited on (001)-oriented STO, we measured the (111) peaks of the NiO layer alongside the substrate's (111) reflections.

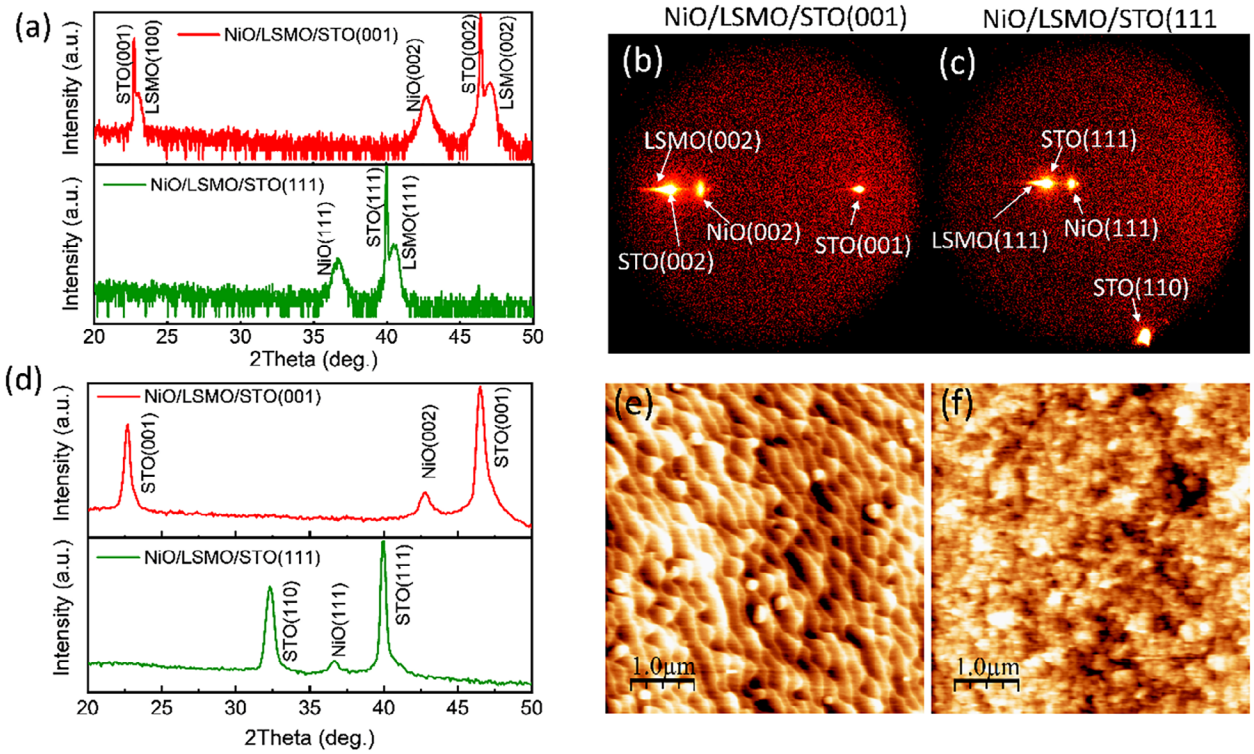

Figure 3. a) High-resolution theta-2theta x-ray diffraction (XRD) pattern of the NiO(25 nm)/LSMO(15 nm)/(001)STO (red) and NiO(25 nm)/LSMO(15 nm)/(111)STO (green). The three-layer structures are characterized by the [001] or [111]-preferential growths, respectively. General area detector diffraction system (GADDS) spectra for b) NiO(25 nm)/LSMO/(001)STO and c) NiO(25 nm)/LSMO/(111)STO. d) 1D theta-2theta XRD signals obtained from GADDS integration, they correlate well with spectra displayed in (a). Due to the lower resolution, STO and LSMO peaks are not resolved. e) Atomic force microscopy topography images of Pt/NiO(1 nm)/LSMO(15 nm) grown on (001)-STO and f) (111)-STO, with RMS surface roughness values below 0.15 nm, indicating atomically smooth surfaces.

Likewise, for NiO grown on (111)-oriented STO, we performed φ-scans using the NiO (200) reflections together with the corresponding STO (200) peaks. In both configurations, the NiO layer was 25 nm thick and was deposited on top of LSMO(15 nm)/STO films.

(001) Substrate: **Figure** 4a,b show XRD pole figures for a 25 nm NiO film grown on LSMO/(001)-STO, showing STO(111) and NiO(111) reflections, respectively. As seen in Figure 4a, the STO substrate produces four sharp {111} peaks, spaced 90° apart, reflecting its cubic symmetry. The NiO(111) pole figure in Figure 4b likewise displays fourfold rotational symmetry, demonstrating that the NiO layer adopts a single in-plane orientation. Extracted φ-scans from the corresponding pole figures (Figure 4c) reveal that each NiO peak aligns perfectly with the corresponding STO peak, confirming perfect matching of crystallographic axes between film and substrate. Together, these data establish a cube-on-cube epitaxy: NiO(001)[100]//STO(001)[100].

(111) Substrate: The STO (200) pole figure, which is inclined at $\psi = 54.74°$ from the sample surface (Figure 4d), exhibits three peaks spaced by 120°, reflecting the substrate's threefold symmetry on its (111) plane. In contrast, the φ-scan of the NiO (200) reflection ($2\theta \approx 43.21°$) in Figure 4e reveals six equally spaced peaks, separated by 60°. Although the {111} planes of cubic NiO intrinsically have threefold symmetry, the appearance of six peaks in the NiO (200) scan indicates that the present NiO films consisted of two-phase domains, one of which was rotated with respect to the other around the [111] axis by 60°. Consequently, the epitaxial relations are (111)[1-10]NiO//(111)[1-10]STO and (111)[1-10]NiO//(111)[10-1]STO. A closer look at the φ-scans (Figure 4f) shows that the stronger set of NiO {200} peaks (domain A) coincides with the STO {200} peaks, (epitaxial relation: (111)[1-10]NiO//(111)[1-10]STO), while a weaker set (domain B) is rotated by 60° (epitaxial realtion: (111)[1-10]NiO//(111)[10-1]STO).

When comparing their intensities on a linear scale, domain A peaks reach ≈10 000 counts, whereas domain B peaks only ≈700 counts with very similar FWHM (Figure S3, Supporting Information). From this, assuming that the diffracted intensity is proportional to the square volume, we infer that domains B constitute ≈20% of the 25 nm NiO film grown on LSMO/(111)-STO.

A schematic ball model illustrating the epitaxial growth driven by the anionic stacking of the FCC lattice of NiO oxygens on top of the close-packed (La,Sr)O planes of LSMO[33] is shown in **Figure** 5.

2.2.3. Reciprocal Space Maps (RSM) of Pt/NiO/LSMO/STO Trilayers

In order to analyze the structural strain of the layers, RSM measurements were performed. Since very thin NiO layers of interest for spintronic applications, typically a few nm, were not

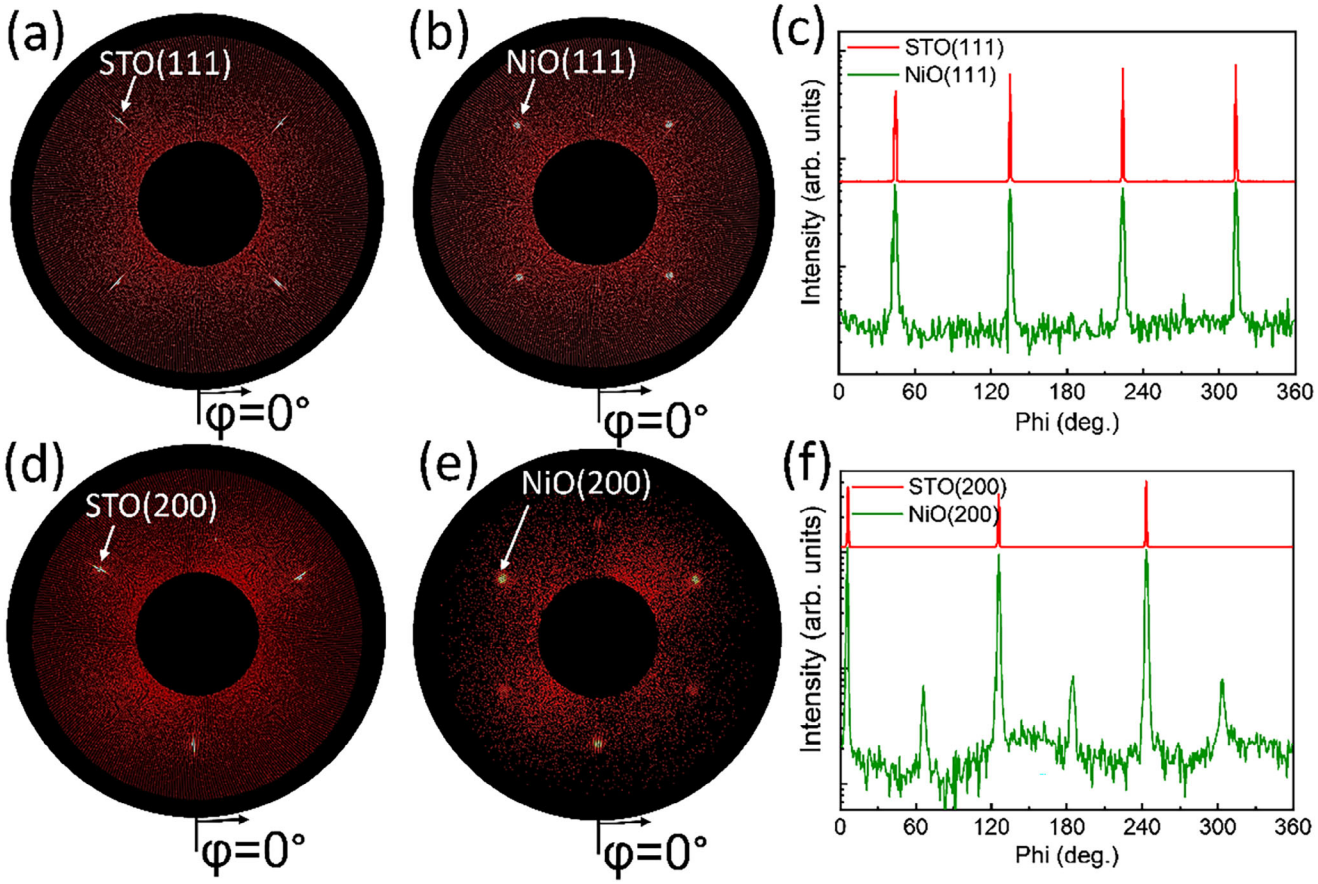

Figure 4. a) Out-of-plane pole figure for the (111) reflections of the (001)-STO substrate and b) of the 25 nm thick NiO film grown on top of LSMO(15 nm)/(001)-STO. c) Extracted phi-scans from graphs (a) and (b) plotted in logarithmic intensity scale. d) Out-of-plane pole figure for the (200) reflections of the (111)-STO substrate, and e) the 25 nm thick NiO film grown on top of LSMO(15 nm)/(111)-STO. f) Phi-scans in logarithmic intensity scale extracted from graphs (d) and (e).

detectable by conventional XRD, these studies were performed on a NiO(25 nm)/LSMO(15 nm)/STO sample. To extract the lattice parameters, RSMs of the STO substrate and NiO film out-of-plane reflections for each substrate orientation were recorded using the GADDS system.

For the (001)-oriented STO substrate, we analyzed the NiO(111) reflections (see **Figure** 6a). Although the STO and LSMO peaks are not fully resolved at this resolution, we determined the NiO in-plane (*ip*) and out-of-plane (*oop*) lattice constants to be $a_{ip}^{NiO} = 4.18(1)$ Å and $a_{oop}^{NiO} = 4.25(1)$ Å, which indicates a cell expansion along the growth direction ($a_{oop} > a_{ip}$). Similarly, on the (111)-STO substrate, we examined the NiO(200) reflections (see Figure 6b) and treated the film as a hexagonal cell with $a_h = 5.90(1)$Å and $c_h = 7.40(1)$Å. Converting these values back to an equivalent cubic cell yields $a_{ip}^{NiO} = a_h/\sqrt{2} = 4.17(1)$ Å and $a_{oop}^{NiO} = c_h/\sqrt{3} = 4.27(1)$ Å respectively, showing again and out-of-plane elongation of the unit cell. This c_h-value corresponds to an interplanar distance of the (111) planes parallel to the film surface, $d^{NiO}_{(111)} = 2.467$ Å, while the estimated interplanar distance for the {11-1} lattice planes is $d^{NiO}_{(11\text{-}1)} = 2.414(6)$ Å. Therefore, thick NiO layers are largely relaxed but retain a measurable out-of-plane distortion ($a_{ip}^{NiO} < a_{oop}^{NiO}$) independently of the substrate orientation. Since these results reflect the strain state of a relatively thick NiO layer (25 nm), the question remains whether the behavior in a NiO layer of a few nm will be the same. To clarify this point, RSMs of Pt/NiO(5 nm)/LSMO(15 nm)/STO heterostructures have been performed using synchrotron diffraction for samples grown on both (001)- and (111)-oriented STO substrates. **Figure** 7a displays the symmetric RSM around the STO(111) reciprocal-lattice point for films on (111)-STO. The coincident peak positions of the substrate, the fully strained LSMO layer, and the NiO film confirm the absence of any macroscopic tilt between these layers. The sharp, vertically elongated intensity at $q_{(11\text{-}2)} = 0$ arises from the overlapping STO(111) and strained LSMO reflections.[34] From this map, we directly extract the interplanar spacing of the (111) planes as $d_{(111)} = 2.451(6)$ Å, in excellent agreement with the $d_{(111)}$ value inferred from our θ–2θ scans (2.449 Å for a 25 nm NiO film). Figure 7b,c show asymmetric RSMs around the (22-2) and (220) reciprocal lattice points of STO, respectively. The elongated contours associated with the NiO reflections reflect the finite 5 nm film thickness. In each map, the solid red line marks the positions compatible with a cubic cell (fully relaxed NiO) while the dashed red line indicates the pseudomorphic (fully strained) positions. NiO diffraction peaks

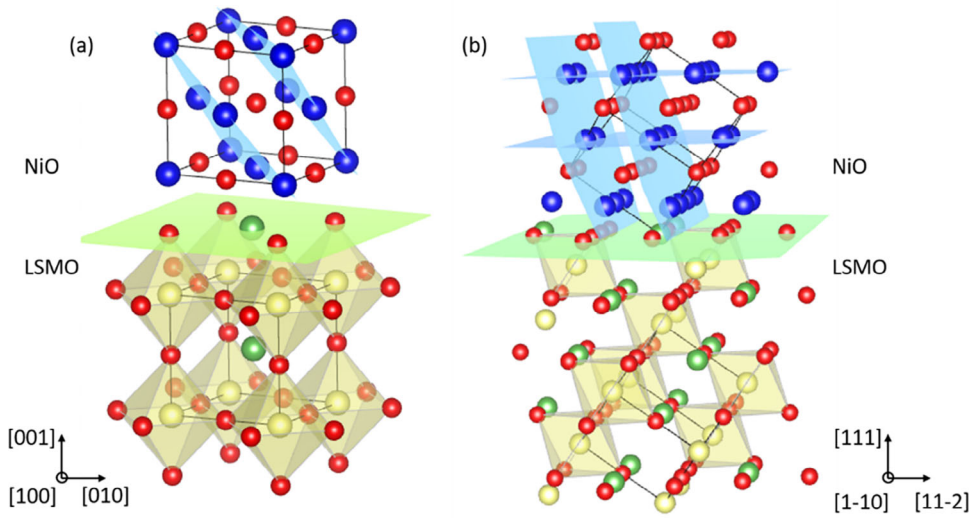

Figure 5. Sketch of the NiO/LSMO bilayers grown on: a) (001)- andb) (111)- orientations. Epitaxial growth is assumed to be governed by the anionic stacking of the FCC lattice of NiO oxygens on top of the close-packed (La,Sr)O planes of LSMO. For simplicity, pseudocubic structures are drawn, neglecting lattice distortions and octahedral tilting. In (a), a (Mn_2)- termination is imposed as the interface layer (green plane), and in (b) a (LaSr) termination is considered. The blue layers indicate antiferromagnetic ordering along (111) planes in NiO. We observe that, in the case of (111) oriented films, at least one of the T-domains lays in the substrate basal plane. On the contrary, for (001)-oriented planes, all magnetic domains are out-of-plane. Atoms are Ni (blue), O (red), Mn (yellow), and La/Sr (green).

appear below the solid red line in both Figure 7b,c. The shift of the NiO layer peak toward the lower $q_{(111)}$ magnitude (i.e., larger out-of-plane lattice parameter) demonstrates the same in-plane compression found for the thicker (25 nm) film.

From the (22-2) reflection, we straightforwardly estimated the interplanar distance of the (11-1) lattice planes (which we assume that is the same than that for the (-111) and (1-11) planes), which are not parallel to the film surface, resulting in $d_{(11\text{-}1)}$ = 2.415(3) Å. This value is shorter than the calculated interplanar spacing for the (111) planes. **Figure 8** provides a schematic representation of the NiO unit cell illustrating this distortion. The expansion of the lattice for the (111)-oriented planes weakens the first neighbors Ni-O-Ni FM superexchange interactions due to the distortion of the Ni–O–Ni bond angles (that depart from 90°).

The estimated equivalent lattice parameters in the cubic notation are a_{ip}^{NiO} = 4.175(5) (a value that closely corresponds with the bulk value a^{NiO} = 4.177 Å), and a_{oop}^{NiO} = 4.239(5) Å, respectively. This indicates that the (111) NiO-oriented films grow with a slight distortion such that $a_{ip}^{NiO} < a_{oop}^{NiO}$.

Similarly, we analyzed the high-resolution RSMs for the NiO(5 nm)/LSMO(15 nm)/ (001)-STO trilayer structures. The symmetric RSM around the STO (002) reflection, shown in **Figure 9a**, confirms the absence of macroscopic tilts between the STO substrate, the LSMO layer, and the NiO thin film. From the symmetric RSM around the STO (002) reflection, we extracted

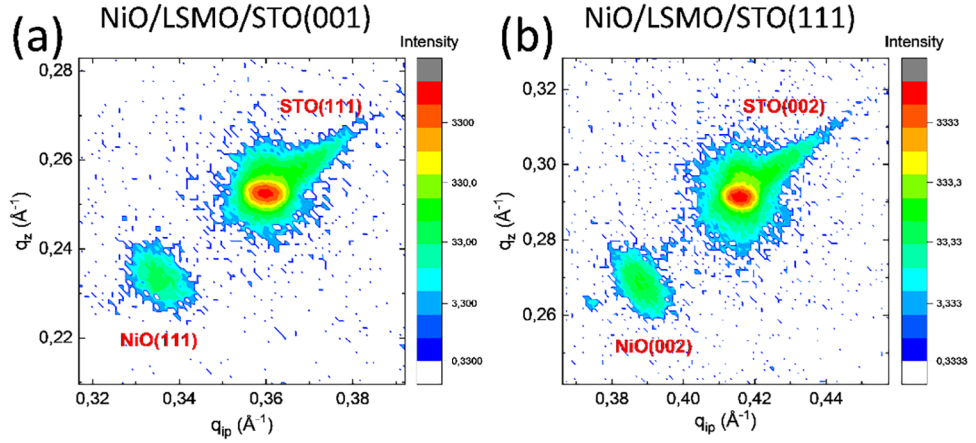

Figure 6. Reciprocal space maps measured with the GADDS system of: a) the STO (111) and NiO (111) reflections for the trilayer structure Pt/NiO(25 nm)/LSMO(15 nm)/(001)-STO; and b) the STO (002) and NiO (002) reflections for the trilayer structure Pt/NiO(25 nm)/LSMO(15 nm) /(111)-STO.

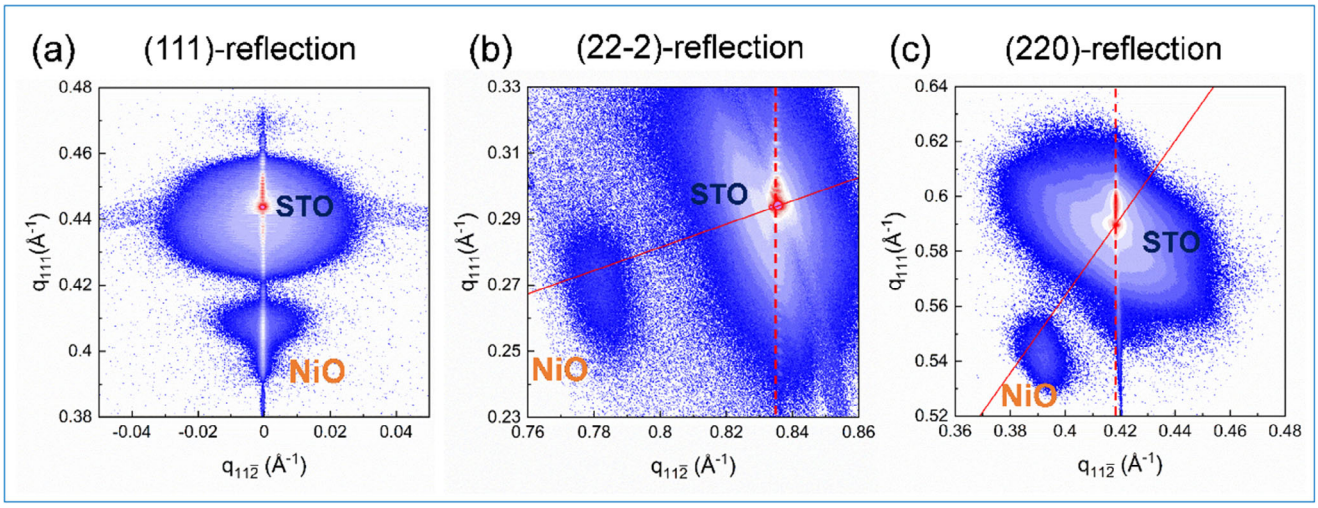

Figure 7. Reciprocal space maps around the a) STO (111) reciprocal lattice point; b) STO (22-2) reciprocal lattice point; and c) the (220) reciprocal lattice point, for the trilayer structure NiO(5 nm)/LSMO(15 nm)/STO-(111) substrate. The fully relaxed and pseudomorphic growth positions of NiO are given by solid and dashed red lines, respectively.

the out-of-plane lattice constant of NiO as $a_{oop}{}^{NiO}$ = 4.24(1) Å. Asymmetric RSMs around the STO (111) and (202) reflections, presented in Figure 9b,c, reveal that the NiO films are highly relaxed, expanding toward their bulk lattice parameter, similar to what was observed on the (111)-oriented STO substrate. As in Figure 7b,c, solid red lines show the positions compatible with a cubic cell (fully relaxed NiO). From these measurements, the in-plane and out-of-plane lattice parameters are determined as $a_{ip}{}^{NiO}$ = 4.18(1) Å (close to the bulk value a^{NiO} = 4.177 Å), and $a_{oop}{}^{NiO}$ = 4.24(1) Å, respectively. These findings indicate that while the 5 nm NiO films grown on LSMO/(001)-STO are largely relaxed, they still exhibit a degree of lattice distortion, as evidenced by the condition $a_{ip}{}^{NiO} < a_{oop}{}^{NiO}$. Notably, these results demonstrate that the unit cell volume is clearly larger than that of bulk NiO in both orientations.

To account for cell distortion, in the case of the (001) orientation, the deviation from a cubic cell can be simply estimated by evaluating the ratio $\epsilon_t = a_{oop}/a_{ip}$ = 1.014 (which corresponds to a 1.4% deviation). For the (111) case, the distortion, ϵ_h, may be estimated by comparing the experimental ratio between c_h/a_h = 1.245 and the expected value for a cubic structure, i.e., $\sqrt{(3/2)}$ = 1.225. We have found ϵ_h = 1.016 (a 1.6% deviation, indicating a slightly higher degree of distortion). Thus, although the distortion values are relatively similar, we should stress that the structural symmetry change between (001) and (111) appears to be significant to account for the different magnetic behaviours.

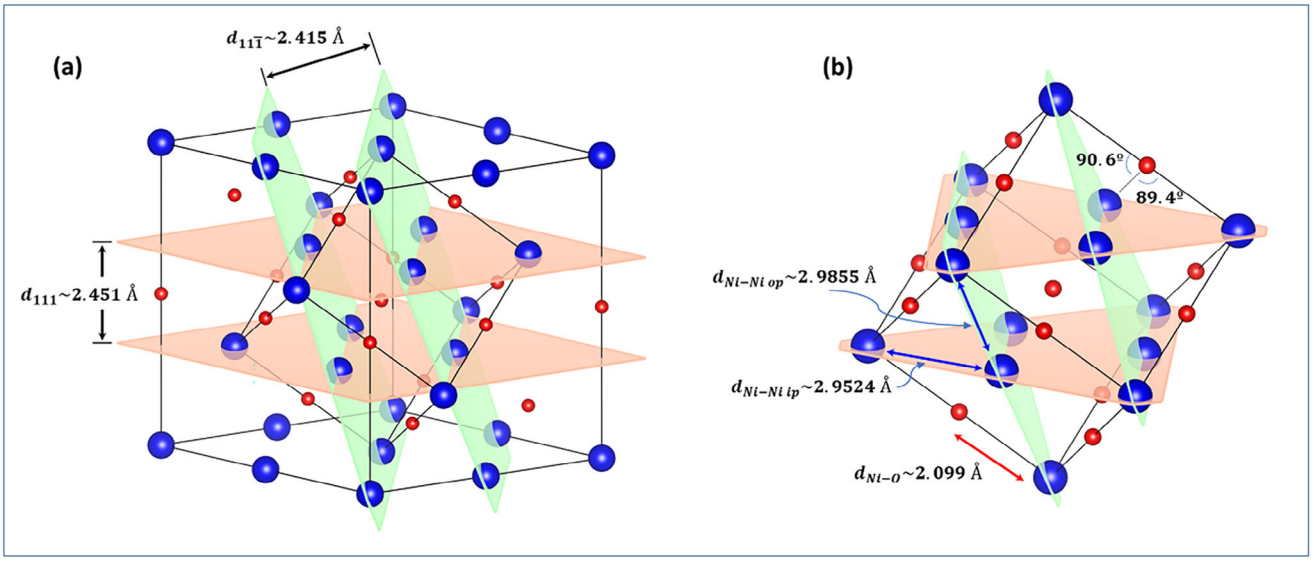

Figure 8. a) Schematic representation of the NiO unit cell, indicating the different interplanar distances between {111} and {11-1} planes, b) Schematic representation displaying the changes in Ni–O and Ni–Ni distances and bond angles extracted from synchrotron diffraction reciprocal space maps.

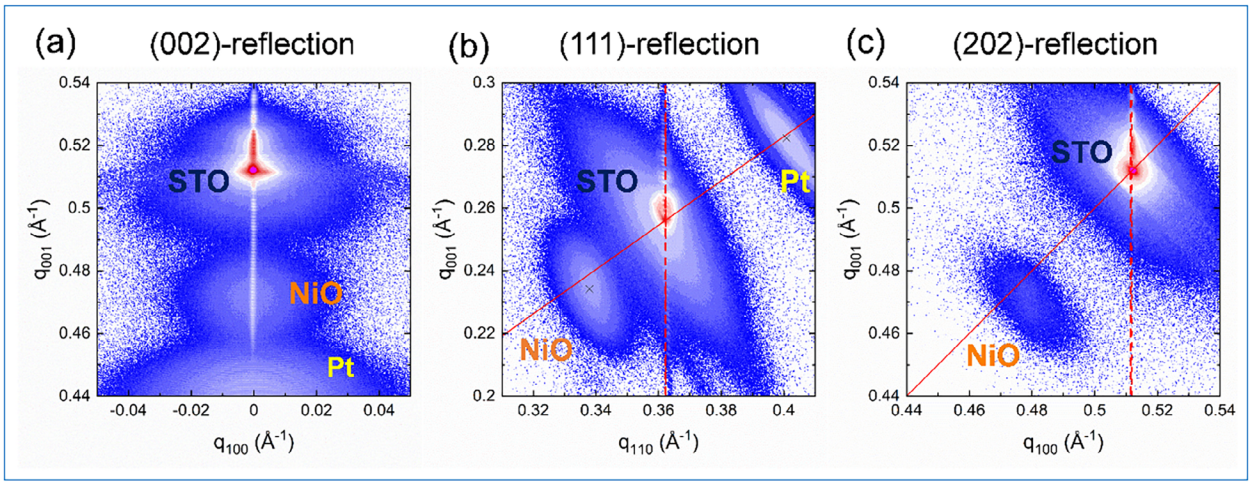

Figure 9. Reciprocal space maps around the a) STO (002) reciprocal lattice point; b) STO (111) reciprocal lattice point; and c) the (202) reciprocal lattice point, for the trilayer structure NiO(5 nm)/LSMO(15 nm)/STO-(001) substrate. The positions of fully relaxed and pseudomorphic growth of NiO are given by solid and dashed red lines, respectively.

To demonstrate the superior spin transmission of (111) oriented NiO layers, we conducted FMR and ISHE measurements. We swept the externally applied magnetic field, H, in the microwave range from 2 to 16 GHz for three different heterostructures: Pt/NiO(1 nm)/LSMO(15 nm)/STO (See Figure S1, the Supporting Information). The NiO layer was either deposited at room temperature (RT) on (001)-STO, resulting in polycrystalline NiO, or at 450 °C on (001)- or (111)-STO substrates, producing epitaxial NiO. As can be seen in **Figure 10**, our results show that the signal amplitude increases from the polycrystalline NiO to the (111)-oriented epitaxial NiO, indicating more effective spin transport through the NiO layer in the latter case. The superior spin conduction efficiency observed in (111)-oriented samples is primarily attributed to a more favorable orientation of the Néel vector and distinct interface symmetry, which together enhance spin-Hall-related effects. An in-depth study of spin conduction mechanisms as a function of crystallinity and crystallographic orientation of the NiO layer, which is beyond the scope of this article, is currently underway and will be published elsewhere.

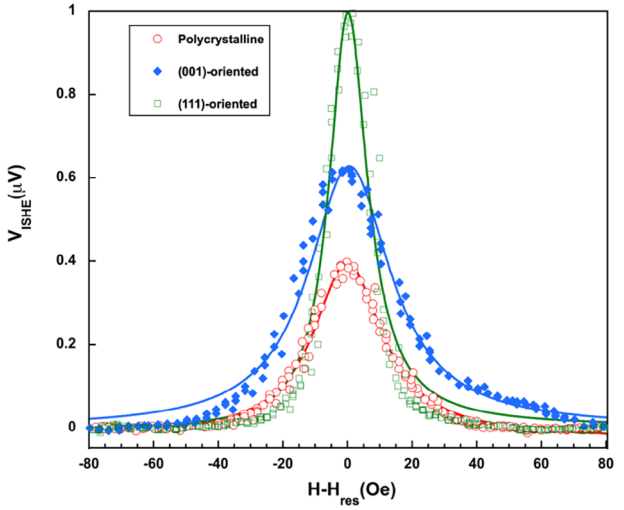

Figure 10. The transverse voltage signal (V_{ISHE}) as a function of the magnetic field at RT and at a resonance frequency of 9 GHz. The data pertains to three different heterostructures composed of Pt/NiO(1 nm)/LSMO(15 nm)/STO, each with distinct characteristics for the NiO layer: polycrystalline, (001) oriented, and (111) oriented, respectively. Solid lines represent the standard fit, including both symmetric and antisymmetric contributions; see, for example, reference.[11]

3. Summary

In this work, we present a detailed study of the structural and microstructural properties of epitaxial NiO thin films, which are of significant interest for AF spintronics development. Our results show that epitaxial NiO films can be grown with excellent crystalline quality on LSMO-capped STO substrates, using both (001) and (111) crystallographic orientations via RF sputtering. Although there is a nominal lattice mismatch of ≈7%, the NiO films achieve coherent growth, with the formation of misfit dislocations occurring specifically at the LSMO/NiO interface. This results in high-quality epitaxial heterostructures with atomically sharp LSMO/NiO interfaces and flat surfaces. Synchrotron RSM reveals that 5 nm NiO films are largely relaxed but still exhibit compressive distortion (where $a_{oop} > a_{ip}$) in both orientations, consistent with XRD data from much thicker (25 nm) layers. Notably, the unit cell volume is clearly larger than that of bulk NiO in both orientations. A key finding is that the substrate orientation dictates the symmetry and domain structure of the NiO layer. For (001)-oriented growth, the NiO forms a single-domain, cube-on-cube alignment with the four {111} planes (giving rise to AF T-domains as in bulk NiO) oblique to the sample plane and therefore, resulting in an out-of-plane Néel-vector orientation. In contrast, (111)-oriented growth produces two in-plane rotational variants, with one being clearly dominant. Further synchrotron RSM analysis shows that, among the four families of {111} planes, the one parallel to the plane of the layers exhibits a greater separation between the FM (111) planes than the others, due to deformation of the NiO unit cell in the (111) direction. This deformation would alter the Ni–O–Ni bond angles at 90°

(relevant for FM interactions) but leave the Ni–O–Ni bonds at 180° (relevant for AF interactions) unchanged. This splitting of the {111} interplanar distances is against the spontaneous structural deformation that takes place in bulk NiO and that defines the T-domains below T_N. This can significantly affect the final magnetic ordering and, consequently, the efficiency of spin transmission through the NiO layer.[18] These findings demonstrate that (001)-oriented NiO films are not optimal for spin transmission. Our results provide a structural framework for tailoring AF domain orientation in NiO, which is directly relevant for optimizing spin-current transmission and magnetic coupling in FM/AF/NM heterostructures.

4. Experimental Section

The LSMO/NiO/Pt heterostructures were deposited on (001)- and (111)-oriented STO substrates using RF magnetron sputtering. The LSMO films, with a thickness of 15 nm, were deposited at 850 °C under a pressure of 140 mTorr in an Ar-O_2 atmosphere. Following deposition, the films were annealed for 1 h at 850 °C in a high-pressure oxygen environment (380 Torr). Subsequently, a series of NiO layers with thicknesses ranging from 1 to 25 nm, were deposited by DC sputtering on top of LSMO films at 450 °C and 50 mTorr pressure in an Ar-O_2 atmosphere from a 0.5 mm thick Ni foil target. Finally, NiO layers were covered with 5 nm thick Pt layers deposited also by DC sputtering at room temperature (RT) and a pressure of 5 mTorr in Ar atmosphere from a Pt foil target.

The structural properties of the epitaxial films were studied by XRD and X-ray reflectivity by using a Bruker D8 Discover four-circle diffractometer with monochromatic $Cu_{K\alpha 1}$ radiation (1.5406 Å) and a Bruker D8 Advance general area detector diffraction system (GADDS). High-resolution 3D RSMs were collected at KMC-II[35] beamline at BESSY-II (Berliner Elektronenspeicherring für Synchrotronstrahlung, Helmholtz Zentrum Berlin) using a monochromatic X-ray beam ($\lambda = 1.5406$ Å). This beamline is equipped with a Bruker Vantec 2000 GAADS. RSMs have been done by scanning the incident angle ω for symmetric diffraction peaks and scanning the azimuthal angle φ for non-symmetric diffraction peaks. The surface roughness of the devices was assessed using atomic force microscopy performed with an Asylum Research MFP-3D microscope in tapping mode. The interfacial microstructure was studied using aberration-corrected STEM on a Thermo Fisher Scientific probe-corrected Titan 60–300 microscope. The instrument was operated at 300 kV and featured a high-brightness Schottky field emission gun (X-FEG), a Wien filter monochromator, a CETCOR aberration corrector for the condenser system (by CEOS), and an Ultim Max TLE10 energy-dispersive X-ray spectroscopy (EDS) system from Oxford Instruments. Atomically resolved Z-contrast images were obtained using HAADF imaging. The probe had a convergence semi-angle of 24 mrad, resulting in a probe size of 1 Å. STEM spectrum line profiles were acquired by combining HAADF imaging with EDS at a beam current of ≈200 pA.[36]

Supporting Information

Supporting Information is available from the Wiley Online Library or from the author.

Acknowledgements

This work has received funding from the State Investigation Agency, through the Severo Ochoa Programme for Centres of Excellence in R&D (CEX2023–001263-S and CEX2023-001286-S) and "OXISOT" (PID2021-128410OB-I00), "AMONANO" (PID2020-112914RB-I00), and HTSU-PERFUN (PID2021-124680OB-I00) funded by MCIN/AEI/ 10.13039/501100011033, from the Gobierno de Aragon project E13_23R, including FEDER funding, and by "ERDF A way of making Europe," by the "European Union." Shoulong Chen acknowledges financial support from the China Scholarship Council (CSC). M. Toda-Casaban acknowledges financial support from the "Spanish Ministry of Science, Innovation and Universities" through a FPU scholarship. The authors thank BESSY-II Synchrotron for providing beamtime (exp. num. 242-12902-ST) and Dr. Daniel Többens for his kind assistance during data collection at the KMC-II beamline. The authors acknowledge the contribution from ICMAB-CSIC's Scientific & Technological Services, specially X-Ray Diffraction (Mr. J. Esquius, Ms. A. Crespi, and Mr. X. Campos). This work has been performed in the framework of the Ph.D. program in Materials Science of the Universitat Autònoma de Barcelona (UAB), through the CSC/UAB Joint Scholarship program.

Conflict of Interest

The authors declare no conflict of interest.

Data Availability Statement

The data that support the findings of this study are available from the corresponding author upon reasonable request.

Keywords

antiferromagnets, complex oxides heterostructures, epitaxial strain, synchrotron radiation techniques, thin films

Received: May 20, 2025
Revised: June 19, 2025
Published online: August 1, 2025

[1] V. Baltz, A. Manchon, M. Tsoi, T. Moriyama, T. Ono, Y. Tserkovnyak, *Rev. Mod. Phys.* **2018**, *90*, 015005.
[2] M. B. Jungfleisch, W. Zhang, A. Hoffmann, *Phys. Lett. A* **2018**, *382*, 865.
[3] D. Hou, Z. Qiu, E. Saitoh, *NPG Asia Mater* **2019**, *11*, 35.
[4] W. Yuan, J. Li, J. Shi, *Appl. Phys. Lett.* **2020**, *117*, 100501.
[5] H. Bai, X. Zhou, Y. Zhou, X. Chen, Y. You, F. Pan, C. Song, *J. Appl. Phys.* **2020**, *128*, 210901.
[6] S. M. Rezende, A. Azevedo, R. L. Rodríguez-Suárez, *J. Appl. Phys.* **2019**, *126*, 151101.
[7] Y. Shiota, T. Taniguchi, D. Hayashi, H. Narita, S. Karube, R. Hisatomi, T. Moriyama, T. Ono, *Nat. Commun.* **2024**, *15*, 9750.
[8] L. Zhu, L. Zhu, R. A. Buhrman, *Phys. Rev. Lett.* **2021**, *126*, 107204.
[9] W. Lin, K. Chen, S. Zhang, C. L. Chien, *Phys. Rev. Lett.* **2016**, *116*, 186601.
[10] H. Wang, J. Finley, P. Zhang, J. Han, J. T. Hou, L. Liu, *Phys. Rev. Appl.* **2019**, *11*, 044070.
[11] S. Chen, A. Pomar, L. Balcells, Z. Konstantinovic, C. Frontera, C. Magén, N. Mestres, B. Martinez, *J. Alloys Compd.* **2025**, *1010*, 177453.
[12] C. Schmitt, L. Baldrati, L. Sanchez-Tejerina, F. Schreiber, A. Ross, M. Filianina, S. Ding, F. Fuhrmann, R. Ramos, F. Maccherozzi, D. Backes, M. A. Mawass, F. Kronast, S. Valencia, *Phys. Rev. Appl.* **2021**, *15*, 034047.
[13] J.-H. Park, E. Vescovo, H.-J. Kim, C. Kwon, R. Ramesh, T. Venkatesan, *Nature* **1998**, *392*, 794.
[14] C. Liu, C. K. A. Mewes, M. Chshiev, T. Mewes, W. H. Butler, *Appl. Phys. Lett.* **2009**, *95*, 022509.
[15] V. Haspot, P. Noël, J. P. Attané, L. Vila, M. Bibes, A. Anane, A. Barthélémy, *Phys. Rev. Mater.* **2022**, *6*, 024406.

[16] S. Chen, A. Pomar, L. Balcells, C. Frontera, N. Mestres, B. Martínez, *Adv. Mater. Interfaces* **2024**, *11*, 2300882.
[17] Y. Tserkovnyak, A. Brataas, G. E. W. Bauer, B. I. Halperin, *Rev. Mod. Phys.* **2005**, *77*, 1375.
[18] S. Chen, A. Pomar, L. l. Balcells, Z. Konstantinovic, B. Bozzo, C. Frontera, C. Magén, N. Mestres, B. Martinez, *J. Alloys Compd.* **2025**, *1010*, 177453.
[19] W. L. Roth, *J. Appl. Phys.* **1960**, *31*, 2000.
[20] M. T. Hutchings, E. J. Samuelsen, *Phys. Rev. B* **1972**, *6*, 3447.
[21] H. P. Rooksby, *Acta Cryst.* **1948**, *1*, 226.
[22] K. Arai, T. Okuda, A. Tanaka, M. Kotsugi, K. Fukumoto, T. Ohkochi, T. Nakamura, T. Matsushita, T. Muro, M. Oura, Y. Senba, H. Ohashi, A. Kakizaki, C. Mitsumata, T. Kinoshita, *Phys. Rev. B* **2012**, *85*, 104418.
[23] I. Sänger, V. V. Pavlov, M. Bayer, M. Fiebig, *Phys. Rev. B* **2006**, *74*, 14440.
[24] T. Yamada, *J. Phys. Soc. Jpn.* **1966**, *31*, 664.
[25] F. L. A. Machado, P. R. T. Ribeiro, J. Holanda, R. L. Rodríguez-Suárez, A. Azevedo, S. M. Rezende, *Phys. Rev. B* **2017**, *95*, 104418.
[26] H. Wang, C. Du, P. C. Hammel, F. Yang, *Phys. Rev. Lett.* **2014**, *113*, 097202.
[27] F. Sandiumenge, J. Santiso, L. Balcells, Z. Konstantinovic, J. Roqueta, A. Pomar, J. P. Espinós, B. Martínez, *Phys. Rev. Lett.* **2013**, *110*, 107206.
[28] J. Santiso, L. Balcells, Z. Konstantinovic, J. Roqueta, P. Ferrer, A. Pomar, B. Martinez, F. Sandiumenge, *Cryst. Eng. Comm.* **2013**, *15*, 3908.
[29] J. L. Maurice, F. Pailloux, A. Barthélémy, O. Durand, D. Imhoff, R. Lyonnet, R. Rocher, J. P. Contour, *Philos. Mag.* **2003**, *83*, 3201.
[30] K. J. O'Shea, D. A. MacLaren, D. McGrouther, D. Schwarzbach, M. Jungbauer, S. Hühn, V. Moshnyaga, R. L. Stamps, *Nano Lett.* **2015**, *15*, 586.
[31] M. Moreau, S. M. Selbach, T. Tybell, *J. Appl. Phys.* **2018**, *124*, 185301.
[32] K. H. L. Zhang, R. Wu, F. Tang, W. Li, F. E. Oropeza, L. Qiao, Y. Du, D. J. Payne, J. L. MacManus-Driscoll, M. G. Blamire, *ACS Appl. Mater. Interfaces* **2017**, *9*, 26549.
[33] F. J. Wong, S. Ramanathan, *J. Vac. Sci. Technol. A* **2014**, *32*, 040801.
[34] J. Santiso, J. Roqueta, N. Bagués, C. Frontera, Z. Konstantinovic, Q. Lu, B. Yildiz, B. Martínez, A. Pomar, L. Balcells, F. Sandiumenge, *ACS Appl. Mater. Interfaces* **2016**, *8*, 16823.
[35] D. M. Többens, S. Zander, *J. Large-Scale Res. Facil.* **2016**, *2*, A49.
[36] M. Watanabe, E. Okunishi, K. Ishizuka, *Microsc. Anal.* **2009**, *5*, 23.

ADVANCED MATERIALS INTERFACES
Open Access

Supporting Information

for *Adv. Mater. Interfaces*, DOI 10.1002/admi.202500452

Strain Relief and Domain Architecture in Epitaxial NiO Films on $La_{2/3}Sr_{1/3}MnO_3/SrTiO_3$ for Spin-Transport Engineering

*Shoulong Chen, Carlos Frontera, Meritxell Toda-Casaban, Alberto Pomar, Lluis Balcells, Zorica Konstantinovic, Cesar Magén, Benjamin Martinez and Narcis Mestres**

Supporting Information

Strain Relief and Domain Architecture in Epitaxial NiO Films on $La_{2/3}Sr_{1/3}MnO_3/SrTiO_3$ for Spin-Transport Engineering

Shoulong Chen[1], Carlos Frontera[1], Meritxell Toda-Casaban[1], Alberto Pomar[1], Lluis Balcells[1], Zorica Konstantinovic[2], Cesar Magén[3], Benjamin Martinez[1] and Narcis Mestres[1*]

[1]Instituto de Ciencia de Materiales de Barcelona. ICMAB-CSIC. Campus Universitario UAB, Bellaterra 08193, Spain.

[2]Center for Solid State Physics and New Materials, Institute of Physics Belgrade, University of Belgrade, Belgrade 11000, Serbia.

[3]Instituto de Nanociencia y Materiales de Aragón (INMA), CSIC-Universidad de Zaragoza, 50009 Zaragoza, Spain.

Corresponding author:
N. Mestres, **E-mail**: narcis.mestres@icmab.es

1. Spin current transmission across the NiO layer, and inverse spin Hall effect (ISHE) measurements

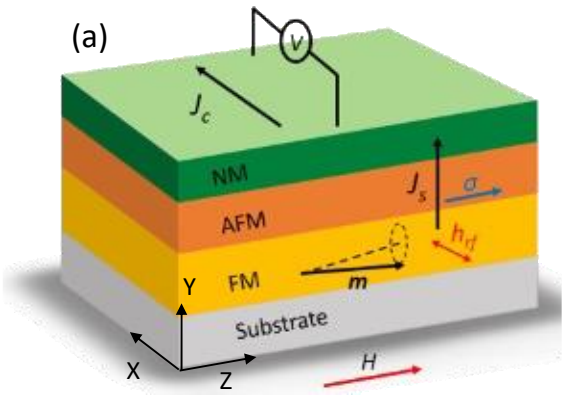

Figure S1. The schematic of the NM/AFM/FM stack shows how spin pumping facilitates the generation and flow of spin current Js across the AFM layer, and the ISHE transverse voltage signal measurements.

2. Magnetic properties and exchange bias

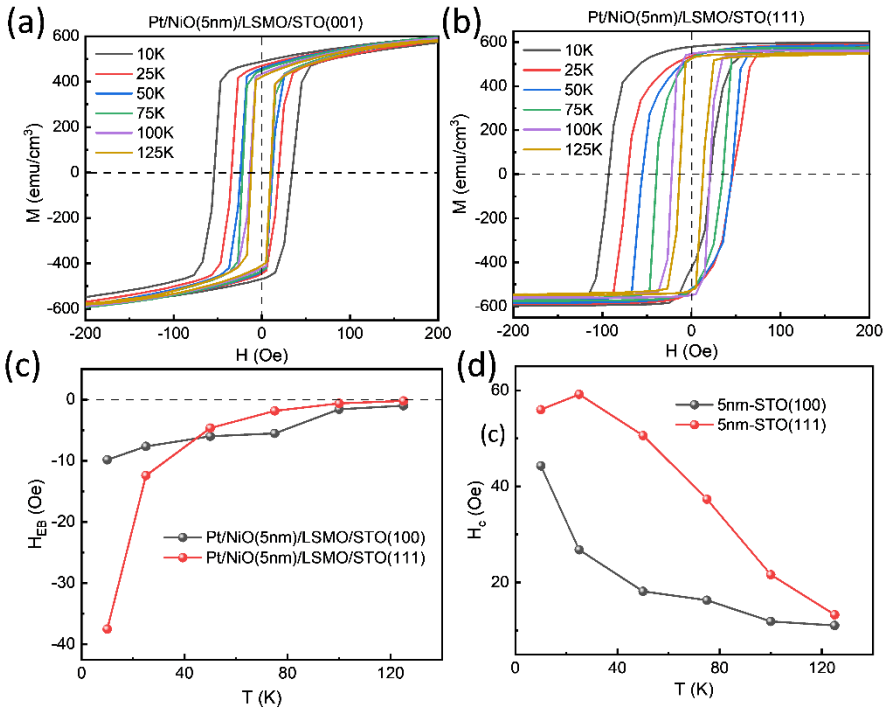

Figure S2. Temperature dependence of the in-plane magnetic hysteresis loops for two Pt/NiO(5 nm)/LSMO(15nm) heterostructures grown on (a) (001)-oriented STO substrate, Ha//(100); and (b) (111)-oriented STO substrate, Ha//(110). (c) Illustrates the temperature dependence of the exchange bias (EB), while panel (d) shows the coercivity field (H_C) for the Pt/NiO/LSMO heterostructures on both (100)- and (111)-STO substrates.

To investigate the magnetic behaviour of the multilayer NiO/LSMO/STO system, static magnetic properties were measured as a function of temperature and magnetic field. In line with the high crystalline quality, LSMO films display a saturation magnetization of $M_S \approx 3.5\ \mu_B$/Mn, which is close to the theoretical value, and ferromagnetic Curie temperatures (T_C) slightly above 350 K. Notably, these properties remain unaffected by the deposition of the NiO layer. Testing antiferromagnetic (AFM) ordering in very thin NiO layers is challenging. This is usually assessed indirectly by observing the occurrence of exchange bias in ferromagnetic (FM)/NiO bilayers. However, this measurement is complicated for LSMO/NiO bilayers because the LSMO layer's T_C may be lower than the T_N of the NiO layer.[1] Nevertheless, T_N decreases as the thickness of the NiO layer (t_{NiO}) is reduced due to finite-size effects, which allows for a more reliable measurement of exchange bias.[2,3]

The magnetic hysteresis loops, *M(H)*, displayed in Figs. S2(a) and S2(b) show a shift along the magnetic field axis at low temperatures, clearly demonstrating the existence of exchange bias and, consequently, AFM ordering in the NiO layer. Additionally, the temperature dependence of the exchange bias field (H_{EB}) is shown in Fig. S2(c). It can be seen that the H_{EB} value of the NiO/LSMO bilayer grown with a (111) orientation is larger than that of the heterostructures grown with a (001) orientation at low temperatures. Moreover, the blocking temperature (T_B)—specific to the FM/AFM exchange-bias interaction—for the 5 nm thick NiO epitaxial films is around 100 K for both orientations. Therefore, T_N should be above this temperature, implying that the samples are paramagnetic well below room temperature. The coercivity field (*Hc*) of the (111)-oriented LSMO is also higher than that of the (001)-oriented films, as seen in Fig. S2(d). This indicates that there is stronger interface exchange coupling in the NiO/LSMO (111)-oriented systems, likely due to the relative orientation of the Néel vector to the magnetic moment of LSMO.

3. XRD pole figures and φ-scans for (111) oriented heterostructures

The (200) pole figure for the (111)-STO substrate Fig. S3(a) exhibits three peaks spaced by 120°, reflecting the substrate's threefold symmetry on its (111) plane.

In contrast, the φ-scan of the NiO (200) reflection ($2\theta \approx 43.21°$) in Fig. S3(b) reveals six equally spaced peaks, separated by 60°. Although the {111} planes of cubic NiO intrinsically have threefold symmetry, the appearance of six peaks in the NiO (200) scan indicates that the present NiO films consisted of two-phase domains, one of which was rotated with respect to the other around the [111] axis by 60º. Consequently, the epitaxial relations are (111)[1-10]NiO//(111)[1-10]STO and (111)[1-10]NiO//(111) [10-1]STO. A closer look at the φ-scans Fig. S3(c), shows that the stronger set of NiO {200} peaks (domain A) coincides with the STO {200} peaks, (epitaxial relation: (111)[1-10]NiO//(111)[1-10]STO), while a weaker set (domain B) is rotated by 60° (epitaxial realtion: (111)[1-10]NiO//(111)[10-1]STO).

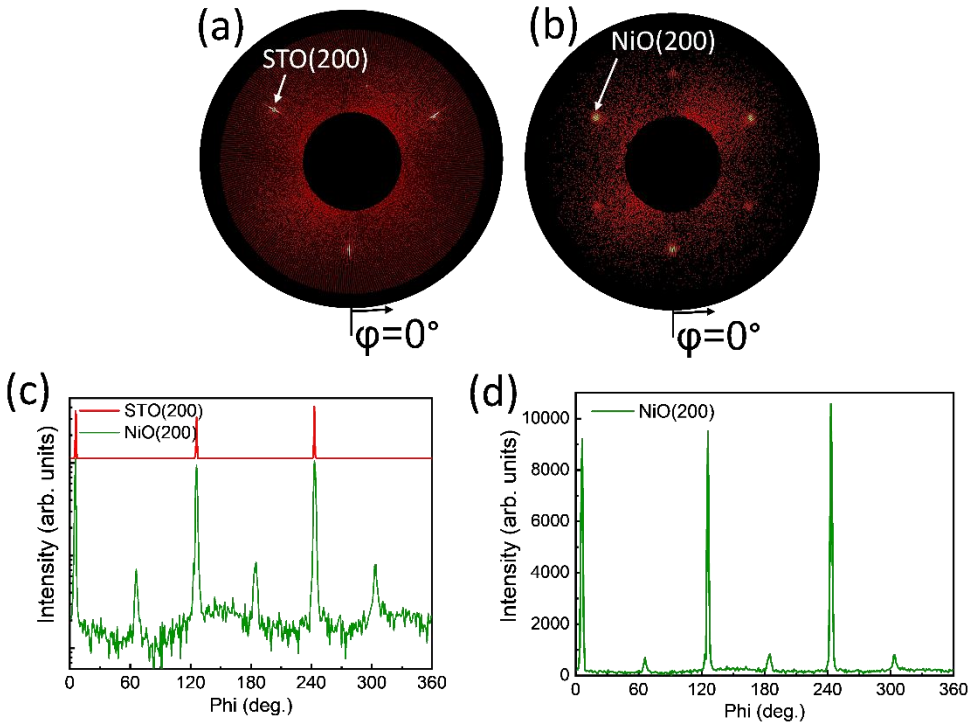

Figure S3: (a) Out-of-plane pole figure for the (200) reflections of the (111)-STO substrate, and (b) the 25 nm thick NiO film grown on top of LSMO(15nm)/(111)-STO. (c) Phi-scans in logarithmic intensity scale extracted from graphs (a) and (b). (d) Phi-scan in linear intensity scale of the NiO (200) reflection for a 25 nm thick NiO film grown on a 15nm LSMO/(111)STO substrate, showing the difference in intensity for the two domains.

When comparing their intensities on a linear scale, domain A reaches approximately 10,000 counts, whereas domain B peaks at only about 700 counts (see Fig. S3(d)). From this, assuming that the diffracted intensity is proportional to the square volume, we infer that domains B constitute around 20% of the 25 nm NiO film grown on LSMO/(111)-STO.

References

1. X.K. Ning, Z.J. Wang, X.G. Zhao, C.W. Shih, Z.D. Zhang, *J. Appl. Phys.* **2013**, *113*, 223903.
2. M. Gruyters, *J. Magn. Magn. Mater.* **2002**, *248*, 248.
3. X.Y. Liang, W.T. Zheng, Q. Jiang, *Nanotechnology* **2007**, *18*, 155701.